Energy Storage Materials 45 (2022) 422–431

Contents lists available at ScienceDirect

Energy Storage Materials

journal homepage: www.elsevier.com/locate/ensm

Correlating the dispersion of Li@Mn_6 superstructure units with the oxygen activation in Li-rich layered cathode

Yiwei Li[a,1], Shenyang Xu[a,1], Wenguang Zhao[a,1], Zhefeng Chen[a], Zhaoxi Chen[b,c], Shunning Li[a], Jiangtao Hu[a], Bo Cao[a], Jianyuan Li[a], Shisheng Zheng[a], Ziwei Chen[a], Taolue Zhang[a], Mingjian Zhang[a,*], Feng Pan[a,*]

[a] School of Advanced Materials, Shenzhen Graduate School, Peking University, Shenzhen 518055, China
[b] Protochips, Inc., 3800 Gateway Centre Blvd. Suite 306, Morrisville, North Carolina 27560, United States
[c] Center for Transformative Science, ShanghaiTech University, Shanghai 201210, China

ARTICLE INFO

Keywords:
Li-rich layered oxide cathode
Li@Mn_6 superstructure units
solid solution process
oxygen activation

ABSTRACT

The oxygen activation, contributing to the high capacity (> 250 mA h g^{-1}) of Li-rich transition metal (TM) layered oxides xLi_2MnO_3•$yLiTMO_2$ (TM = Mn, Ni, Co, Fe, etc.), is rooted in the unique 180° Li-O-Li configuration due to the ordering arrangement of Li@Mn_6 superstructure units in Li_2MnO_3 component (equivalent to $Li[Li_{1/3}Mn_{2/3}]O_2$), but the relationship between the oxygen activation and the distribution of Li@Mn_6 superstructure units has not established. Herein, we comprehensively investigated the dispersion behavior of Li@Mn_6 superstructure units during the synthesis of a model compound $Li[Li_{1/6}Mn_{1/3}Ni_{1/3}Sb_{1/6}]O_2$ (0.5 $Li[Li_{2/3}Mn_{1/3}]O_2$•0.5 $Li[Ni_{2/3}Sb_{1/3}]O_2$) combining *ex-situ* X-ray diffraction (XRD) and *in-situ/ex-situ* transmission electron microscope (TEM). It revealed the entire process from the formation of Li@Mn_6 superstructure units, to the gradual fusion with Sb@Ni_6 superstructure units, eventually to the complete dispersion at 1100 °C. The systemic electrochemical tests demonstrated that, the dispersion of Li@Mn_6 superstructure units effectively suppressed the irreversible oxygen activation, and the best capacity and voltage retentions were obtained in the solid solution with the complete dispersion of Li@Mn_6 superstructure units. This work benefits the design of high performance Li-rich layered oxides with the modest anionic redox activity through the local structural tuning.

1. Introduction

The requirement for the next-generation sustainable and clean energy has become more and more crucial facing to the exhausted fossil fuels. Correspondingly, it demands more advanced energy storage techniques [1–3]. Lithium ion batteries (LIBs), owing to the high energy density and the environmentally friendly characters, have been widely utilized in electronic devices and electric vehicles [4–6]. Nevertheless, the higher energy density and better cycling stability have been pursued for the next-generation LIBs [7]. The energy density of LIB system is largely decided by the cathode materials [8]. Compared with the other cathode materials, Li-rich layered oxides, written as xLi_2MnO_3•$yLiMO_2$ (M = Mn, Ni, Co, Fe, etc.), are considered as the next-generation cathode due to their high specific capacity (> 250 mA h g^{-1}) and high energy density (> 900 mW h g^{-1}) [9–11].

The high capacity of Li-rich cathodes is originated from the special anion redox. Guo et al. found that the extra-capacity of Li-rich cathodes was originated from the oxygen activation [12,13]. The lattice oxygen O^{2-} would be oxidized to form the O-O dimers O_2^{n-} while charging to high voltage, demonstrating the reversible O^{2-}/O_2^{n-} redox in Li-rich cathodes [14–16]. However, the oxygen loss in the form of O_2 or Li_2O from the surface of Li-rich cathodes was also widely reported [17,18]. Ye et al. demonstrated the oxygen loss contributed more capacity than the reversible oxygen redox in the first charge process [19]. It not only leads to the low initial Coulombic efficiency, but also causes the migration of transition metal (TM) cations and the structural degradation from layered to spinel phase [20–22]. The phase transition could be observed both on the surface and in the bulk, causing the continuous capacity and voltage degradation with cycling. The oxygen loss is originated from the irreversible oxygen activation in Li_2MnO_3 part of Li-rich cathodes: Zhuo et al. recently revealed that, oxygen in Li_2MnO_3 processed a too high electrochemical activity to have none reversible oxygen redox [23]. In contrast, the complex with $LiTMO_2$ in Li-rich layered oxides could suppress the irreversible oxygen activation partially,

* Corresponding authors.
E-mail addresses: zhangmj@pkusz.edu.cn (M. Zhang), panfeng@pkusz.edu.cn (F. Pan).
[1] These authors contributed equally to this work.

https://doi.org/10.1016/j.ensm.2021.12.003
Received 29 June 2021; Received in revised form 24 November 2021; Accepted 2 December 2021
Available online 5 December 2021

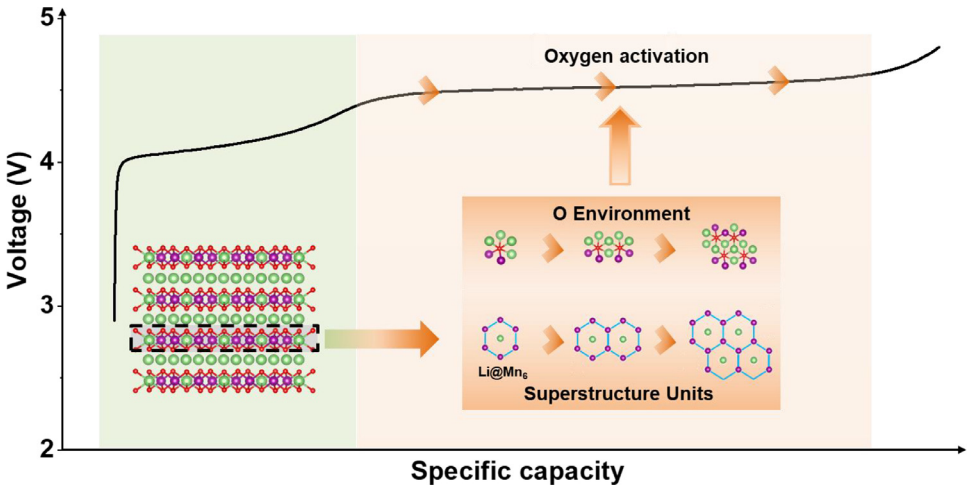

Scheme 1. Illustration of tuning the dispersion of Li@Mn_6 superstructure units to regulate the oxygen activation behavior in Li-rich layered oxide cathodes.

and increase the proportion of the reversible oxygen redox. Therefore, to further suppress the irreversible oxygen activation in Li_2MnO_3 part of Li-rich cathodes is essential to eliminate the negative electrochemical impacts.

The electrochemical behavior of the cathodes is largely related to their crystal structure. In the typical Li-rich cathodes, the electrochemical behavior could be divided into two parts, TM redox part and oxygen redox part [24,25]. The latter is originated from the unique 180° Li-O-Li configuration due to the Li@Mn_6 superstructure unit in TM layers. The previous reports discovered that the oxygen activation process and the electrochemical performance of Li-rich cathodes were determined by the arrangement of the Li_2MnO_3 domains [26–29]. Zuo et al. demonstrated that the better electrochemical properties could be obtained by tuning the distribution of Li_2MnO_3 domain (equivalent to $Li[Li_{1/3}Mn_{2/3}]O_2$) in Li-rich cathode [30]. Hwang et al. discovered that the more reversible oxygen redox could be obtained by more dispersed Li_2MnO_3 domain in Li-rich cathodes [28,29]. Thus, we can deduce that, the edge-sharing arrangement of Li@Mn_6 units in Li_2MnO_3 domain would lead to over-active O configuration, while the dispersion of Li@Mn_6 units in TM layers of Li-rich layered oxides could suppress the irreversible oxygen activation. In another word, the dispersion of Li@Mn_6 units may be related to the oxygen activation process (Scheme 1). It has been reported that the dispersion behavior of the Li@Mn_6 superstructure units in Li-rich oxides is closely related to the synthesis process [31–33]. Until now, the structural evolution of Li-rich oxides during synthesis has been reported from the viewpoint of the phase analysis, however, the dispersion process of Li@Mn_6 superstructure unit and the corresponding influences on electrochemical performance have not been clarified [34,35]

In this work, we took Li-rich oxide $Li[Li_{1/6}Mn_{1/3}Ni_{1/3}Sb_{1/6}]O_2$ (LMNSO) (composed of $Li[Li_{1/3}Mn_{2/3}]O_2$ (LMO) and $Li[Ni_{2/3}Sb_{1/3}]O_2$ (LNSO) with the ratio of 1:1) as an ideal model composite compound to investigate the dispersion process of Li@Mn_6 superstructure units during the synthesis, considering the big difference in the atomic weight between Sb and Ni/Mn. Combining *ex-situ* X-ray diffraction (XRD), *ex-situ* transmission electron microscope (TEM), and *in-situ* TEM, the detailed evolution from the phase segregation to the particle growth, then to the particle merging, and finally to the phase merging, were clearly demonstrated. The electrochemical behaviors of these intermediates with different dispersion extents of Li@Mn_6 superstructure units further confirmed that, the irreversible oxygen activation could be greatly suppressed by the uniform dispersion of Li@Mn_6 units, thereby enhancing the reversibility of oxygen redox, and the better cycling stability and the lower voltage decay could be achieved. These findings provide a deeper understanding into the formation and evolution of Li@Mn_6 superstructure units and the relationship with electrochemical performance in Li-rich cathodes.

2. Experimental

2.1. Preparation of LMNSO, LMO and LNSO

LMNSO was synthesized by sol-gel method. In a typical process, $C_2H_3O_2Li{\cdot}2H_2O$, $NiC_4H_6O_4{\cdot}4H_2O$, $C_6H_9O_6Sb$ and $C_4H_6MnO_4{\cdot}4H_2O$ (Sinopharm Chemical Reagent Co., Ltd) in the stoichiometric ratio were mixed in deionized water. Citric acid and polyvinylpyrrolidone (PVP-K30) (Aladdin Reagent Co., Ltd) were chosen as the chelating agent in the ratio of 1:1. The solution was stirred at 90 °C until it transformed to a colloid. Then the sample was calcined at 140 °C for 3 h, at 500 °C for 3 h and naturally cooled to room temperature to get the precursor. The precursor was calcined at 600, 700, 800, 900, 1000, and 1100 °C for 20, 18, 15, 12, 10, 6 h, respectively, to obtain LMNSO-600, LMNSO-700, LMNSO-800, LMNSO-900, LMNSO-1000 and LMNSO-1100. A series of LMO-LNSO solid solution in different ratios, including LMNSO14 (LMO:LNSO=1:4), LMNSO12 (LMO:LNSO=1:2), LMNSO21 (LMO:LNSO=2:1) and LMNSO41 (LMO:LNSO=4:1), were synthesized by sol-gel method. The synthetic process was similar with the LMNSO-1100. Li_2CO_3 (Aladdin) and Mn_3O_4 (Aladdin) were mechanically mixed in the molar ratio of 3:1 and annealed at 800 °C to obtain LMO. Li_2CO_3 (Aladdin), NiO (Aladdin) and Sb_2O_3 (Aladdin) were mechanically mixed in the molar ratio of 3:4:1 and annealed at 800 °C to obtain LNSO.

2.2. Materials characterization

The crystal structures of LMO, LNSO and LMNSO were characterized by high power XRD collected by Bruker D8-Advance diffractometer using Cu-*Kα* radiation at 50 kV and 100 mA. Rietveld refinements of XRD patterns were carried out using the General Structure Analysis Software (GSAS) package with the EXPGUI interface [36,37]. The particle morphology and element distribution information were obtained by scanning electron microscope (SEM, ZEISS Supra 55 field emission scanning electron microscopy) with energy dispersive spectrometer (EDS). The local structure and the corresponding element distribution were characterized by high-resolution field-emission transmission electron microscopy (FETEM; JEOL-3200FS, 300 kV) with energy dispersive spectrometer (EDS). *In-situ* differential electrochemical mass spectrometry (DEMS) measurements were taken on a customized DEMS device. The DEMS cells initially rested for 3 h and the galvanostatic charge/discharge was performed using a Solartron electrochemical workstation. Atomic resolution high angle annular dark field scanning transmission electron microscope (HAADF-STEM) images were obtained by a FEI Titan 80–300 scanning/transmission electron microscope operated at 300 kV, equipped with a probe spherical aberration corrector. The thermal analysis of the precursor was performed by thermogravimetric analyzer

(TGA, Mettler Toledo) and differential thermal analyzer (DTA) from 500 to 1100 °C with a heating rate of 10 °C min^{-1} under air flow. The inductively coupled plasma-optical emission spectroscopy (ICP-OES, JY2000-2, Horiba Jobin Yvon) was used to analyze the elemental composition.

2.3. Electrochemical tests

Coin-type (CR2032) half cells were assembled to perform the electrochemical measurements. Active material, polyvinylidene fluoride (PVDF) and acetylene black were ground in the ratio of 7:2:1, then mixed with N-methyl pyrrolidone (NMP). The mixture was stirred for 10 h to form a uniform slurry, which was blade-casted on the Al foil and dried at 120 °C in vacuum for 12 h. 1 M $LiPF_6$ and 0.02 M lithium difluoro oxalate borate (LiDFOB) in fluoroethylene carbonate/ hydrofluoroether/ fluoromethyl ethyl carbonate (FEC/HFE/FMEC) mixed solvent was utilized as the electrolyte. The galvanostatic charge-discharge tests were performed using a NEWARE system. Cyclic voltammetry (CV) and electrochemical impedance spectroscopy (EIS) results were obtained by Solartron workstation (1400 cell test system).

2.4. In-situ *TEM experiments*

In-situ observation was performed to examine changes in the morphology and structure of LMNSO during the calcination from room temperature to 1000 °C using field emission spherical aberration transmission electron microscope (GrandARM300F) at an accelerating voltage of 300 kV. AXON System was used to calibrate image drift and contrast changes during the heating process. A heating holder (E-chips, Protochips) with great mechanical stability and ultrahigh temperature stability (< 0.05 °C) was adopted for increasing the temperature from room temperature to 1000 °C with a heating rate of 1 °C/min. At certain temperatures, aberrated high resolution TEM images were recorded. The highly stable heating holder with powerful AXON system ensures the success of *in-situ* observation of local structural evolution with the super-high time and spatial resolution (up to 0.1 Å and millisecond level) during the calcination. Electron energy loss spectroscopy (EELS) mapping was carried out to check the element distribution when holding at 600 °C.

2.5. Computational method

All the calculations were performed using the plane-wave based density functional theory (DFT) method as implemented in the Vienna ab initio simulation package (VASP) [38–41]. Projector augmented wave (PAW) potentials were used to probe valence-core interactions [42,43]. The generalized gradient approximation (GGA) with the Perdew–Burke–Ernzerhof (PBE) functional was chosen as the exchange correlation potential [44]. A cutoff energy was set as 520 eV and the electronic energy convergence criterion was set at 10^{-6} eV. In all the calculations, the Brillouin zone was sampled by Monkhorst-Pack *k*-point grid with density of at least 1000/(the number of atoms per cell). In order to correctly characterize the localization of transition-metal *d*-electrons, The GGA+U method was used to account for the strong correlation in the calculations [45,46]. The values for the Hubbard U parameter for Mn and Ni was 4.2 and 6.7 eV, respectively [47,48]. Geometries were optimized until the forces on the atoms were less than 0.01 eV/Å. The spin-polarized calculations were considered in all our calculations. All calculations were performed considering a ferromagnetic ordering of transition metal atoms.

To examine the thermodynamic stability of oxygen we calculated the oxygen vacancy formation enthalpy ΔH_O, which is given by:

$$\Delta H_O = E\left(Li_xTMO_{2-\delta}\right) + \frac{\delta}{2}E\left(O_2\right) - E\left(Li_xTMO_2\right)$$

Where $E(Li_xTMO_{2-\delta})$ and $E(Li_xTMO_2)$ are the internal energies of the transition metal oxides with oxygen vacancy and without oxygen vacancy, respectively, and $E(O_2)$ is the internal energy of oxygen molecule. To correct the self-interaction errors within DFT, a -1.36eV energy correction for O_2 molecule was used in all our calculations [49].

3. Results and discussions

3.1. The solid solution process between LMO and LNSO

The ICP-OES measurement results of LMNSO annealed at 900, 1000 and 1100 °C are shown in Table S1. The practical element contents are well consistent with the theoretical values. It is worth noting that only about 2% Li-deficiency from 900 to 1100 °C, indicating that little Li loss occurred at high temperatures. Similar XRD patterns of LMO and LNSO (Fig. S1) indicate the similar crystal structure (O3, S. G. *C*2/*m*): Li slab and TM slab alternatively stack along *c* direction (the insets of Fig. S1). The only difference is in the TM layer. The TM layer in LMO is composed of edge-sharing $Li@Mn_6$ superstructure units, while that for LNSO is composed of edge-sharing $Sb@Ni_6$ superstructure units, which could be reflected by different superlattice peaks (marked by the dashed rectangles in Fig. S1). The similar crystal structures make it feasible for the solid solution between these two oxides.

XRD patterns were performed on the LMNSO samples calcined at different temperatures to track the solid solution process (Figs. 1**a**,b and S2,S3) and the corresponding Rietveld refinement results are shown in Fig. S4 (the detailed refinement parameters are summarized in Table S2 and plotted in Fig. 1c–f, respectively). In Fig. S2a, a few extra peaks could be found except for the peaks of Li_2MnO_3, demonstrating some impurities in precursor, which could also be found in TEM images (Fig. S2b,c). In Fig. S2d, the peaks can be indexed to LMO and NiO, implying that, LMO formed prior to LNSO at 600 °C. TEM images of LMNSO-600 in Fig. S2e,f can also confirm the formation of LMO. When calcined at 700 °C, there are two sets of (001) and (131) peaks enlarged in Fig. 1b. The left set can be assigned to LNSO, and the right one belongs to LMO, hinting the formation of LNSO and the coexistence with LMO. As the temperature increases to 800 °C, the widths of the (001) and (131) peaks for LMO and LNSO become narrow, demonstrating the crystal growth and the enhancement of the crystallinity, which could also be reflected by the increased grain size (Fig. 1e). When the temperature is higher than 800 °C, lattice parameters for LNSO continuously increase (Fig. 1d), while lattice parameters for LMO show the reverse trend (Fig. 1c), implying the solid solution process initiates at 800 °C. For LMNSO-900 and LMNSO-1000, the (001) peaks of LMO and LNSO shift to each other, similar with the (131) peaks, which might imply the solid solution process of two phases. It is worth noting that the intensity for (001) and (131) peaks of LMO decreases and the corresponding peak intensity for LNSO increases, implying that, LMO merges into LNSO with the increased temperature. The phase composition changes of LMO and LNSO follow the similar trend as the grain size (Fig. 1f). While the temperature reaches to 1100 °C, there is only one set of (001) and (131) peaks, demonstrating the fully solid solution. The structure evolution process can also be validated by the changes of superlattice peaks (Fig. S3).

In brief, LMO and LNSO formed individually at 600 and 700 °C, respectively. From 700 to 800 °C, they grew up separately. Then the solid solution process between two phases occurred above 800 °C, and LMO constantly merged into LNSO with the increased temperature. Eventually, the fully solid solution formed at 1100 °C, preserving the same layered structure with the parent component.

To further confirm the solid solution process at atomic scale, the *in-situ* TEM images of LMNSO from 700.8 to 977.3 °C (Figs. S5,S6) and the *ex-situ* TEM images with the corresponding EDS were performed on LMNSO-700, LMNSO-800, LMNSO-900, LMNSO-1000, and LMNSO-1100 (Fig. 2). As shown in Fig. S6b, with the increased temperature, LMO particles marked by yellow arrows (according to the contrast difference) gradually fused and grew up, and produced three LMO particles about 20 nm till 729.8 °C, related with the crystal growth process. While the temperature further increasing, the fusion between LMO and

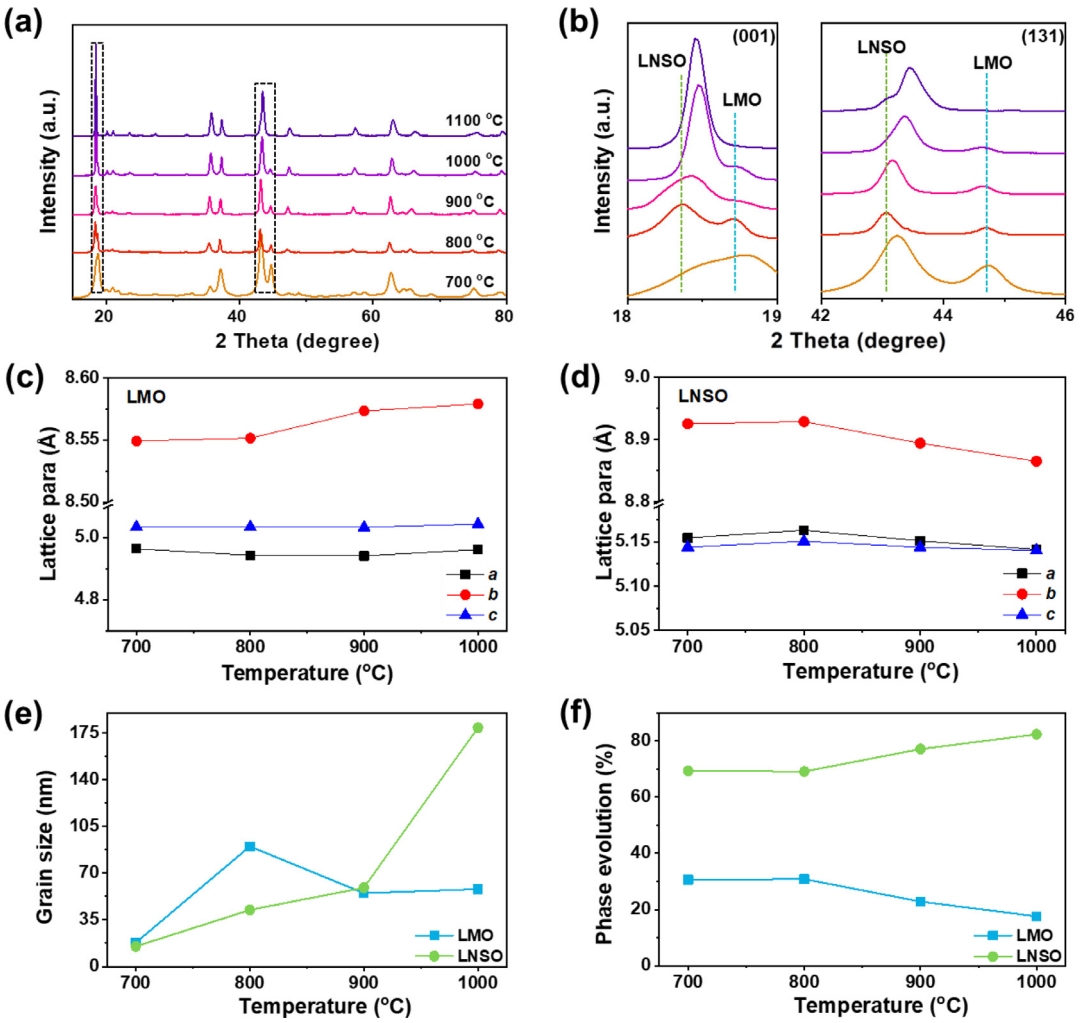

Fig. 1. Tracking the solid solution process from the macroscopic structural analysis. (a) XRD patterns of the as-prepared oxides LMNSO-700, LMNSO-800, LMNSO-900, LMNSO-1000, and LMNSO-1100 and (b) the enlarged (001) and (131) peaks. The change of the refinement parameters *a, b*, and *c* for (c) LMO and (d) LNSO. (e) The grain size and (f) the corresponding phase proportion of LMO and LNSO with the increased temperature according to the refinement results.

LNSO particles gradually proceeded (marked by red arrows and purple arrows in Fig. S6c and 6d, respectively) and lasted until 977.3 °C, which is consistent with the XRD results (Fig. 1) and DTA curve (Fig. S7). The similar phenomenon could also be observed in Fig. 2: Ni and Sb segregation from Mn were observed (Fig. 2a–c), both of which corresponded to the layered structure (Fig. 2f), confirming the separation of LNSO and LMO particles. The segregation gradually disappeared with the increased temperature (Fig. 2d), implying the continuous solid solution process, which was well consistent with the *in-situ* TEM results (Figs. S5 and S6). In addition, with the further increased temperature from 1000 to 1100 °C, as shown in Fig. 2e, Mn, Ni and Sb uniformly distributed in all the particles and the particle exhibited layered structure (Fig. 2f), demonstrating the phase fusion process (related to the endothermic peak appeared at around 1020 °C in DTA curve, Fig. S7), and the solid solution formed at 1100 °C. The whole solid solution process observed by *ex-situ* TEM images and the corresponding EDS spectra are well consistent with the XRD and *in-situ* TEM results. SEM images accompanied with the corresponding EDS spectra for LMNSO-700, LMNSO-800, LMNSO-900, LMNSO-1000, and LMNSO-1100 are shown in Fig. S8, demonstrating the similar results.

Combining XRD and *in-situ/ex-situ* TEM with the corresponding EDS results together, the solid solution process could be summarized in Fig. 2g. From 500 to 700 °C, Li ions were inserted into the metal oxide precursors, and layered LMO and LNSO formed sequentially, corresponding to the phase nucleation process. From 700 to 800 °C, LMO and LNSO small grains (10–30 nm) fused and grew separately to form the larger particles (>100 nm), corresponding to the particle growth process. The particle fusion initiated above 800 °C, LMO particles fast migrated into LNSO particles to form heterogeneous particles. While further increasing the temperature from 1000 to 1100 °C, LMO part and LNSO part in the same heterogeneous particle completed the full phase fusion at the atomic level, forming the solid solution at 1100 °C.

3.2. The dispersion of Li@Mn_6 superstructure units in LMNSO solid solution

Based on the above results, the LMNSO samples calcined at different temperatures can be divided into three categories according to the dispersion extent of Li@Mn_6 superstructure units. (1) LMNSO-700 and LMNSO-800 have no dispersion of Li@Mn_6 superstructure units, since LMO particles segregated from LNSO particles. (2) LMNSO-900 and LMNSO-1000 have a small dispersion of Li@Mn_6 superstructure units since the solid solution process partially occurred at the phase boundary of LMO and LNSO. (3) LMNSO-1100 has a highest dispersion of Li@Mn_6 superstructure units.

To check the final dispersion degree of Li@Mn_6 superstructure units in the solid solution LMNSO-1100, the detailed structure analysis was performed. First, Rietveld refinement was performed on XRD pattern of

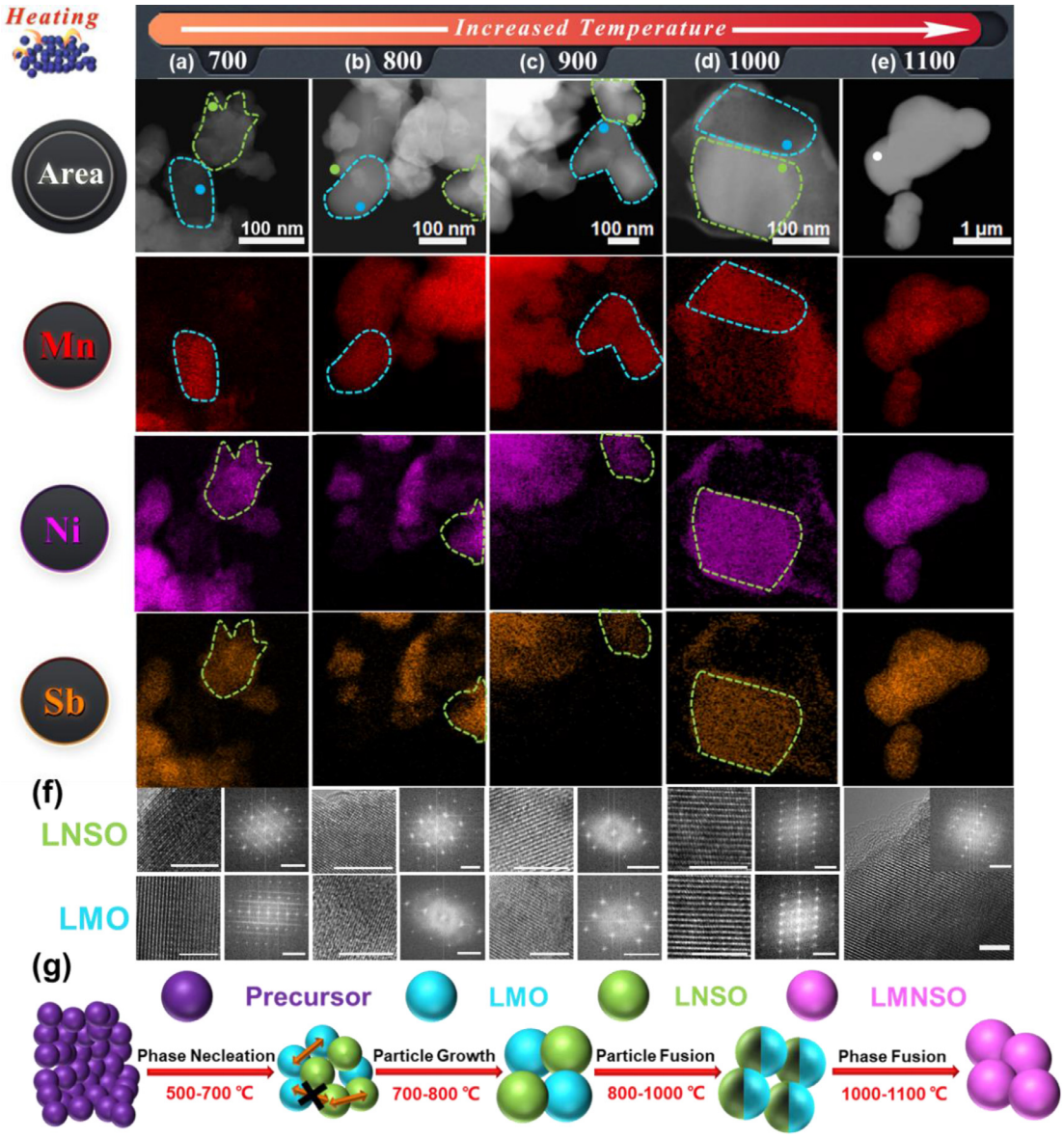

Fig. 2. Monitoring the solid solution process from the local elemental distribution. *Ex-situ* TEM images and the corresponding EDS spectra of Mn, Ni, and Sb of (a) LMNSO-700, (b) LMNSO-800, (c) LMNSO-900, (d) LMNSO-1000 and (e) LMNSO-1100. The aggregated LMO and LNSO particles are marked by blue dashed lines and green dashed lines respectively in LMNSO-700, LMNSO-800 and LMNSO-900. The LMO domain and LNSO domain in LMNSO-1000 are marked by blue dashed lines and green dashed lines, respectively. (f) The HRTEM images recorded from the regions marked by the spots in the corresponding TEM images, and the corresponding FFT maps. The scale bars of HRTEM images and FFT maps are 5 nm and 5 1/nm. The HRTEM images are enlarged in Fig. S9. (g) Illustration of the crystal growth and solid solution process of LMO and LNSO from 500 to 1100 °C.

LMNSO-1100 using a single monoclinic phase (S. G. *C*2/*m*) (Fig. 3a). The well match between the experimental result and simulated result means the absolute solid solution of LMO and LNSO. The superlattice peaks marked by the grey dashed rectangle in Fig. 3**a** were magnified in the inset.

Two extra weak peaks marked by the arrows could be observed, which might be attributed to the short-range ordering of Li@Mn_6 and Sb@Ni_6 superstructure units in TM layers (Fig. S10). To further explore the atomic structure of TM layers, Cs-corrected STEM was performed for LMNSO-1100 (Fig. 3b,c). As shown in Fig. 3b, bright and dark atomic layers alternately arrange, which can be assigned to TM slabs and Li slabs, respectively. The distance between two TM slabs is 5.06 Å, which is well consistent with the refined parameter *c* in Table S2. Considering the big contrast difference between Li and Sb, alternated bright and dark dots should be observed in TM layers along [010] direction if Li@Mn_6 and Sb@Ni_6 superstructure units segregated into nanodomains. Actually, there is no obvious contrast difference in TM layers along [010] direction (Fig. 3b), demonstrating the uniform dispersion of Li@Mn_6 into Sb@Ni_6 superstructure units. To further check the result, the HADDF-STEM image was taken along [301] direction (Fig. 3c). In the ideal solid solution model, two Ni/Mn mixing atomic layers and one Li/Sb mixing atomic layer should arrange alternately along [301] direction (inset of Figs. 3c and S11). The electron scattering cross sections for Li, Mn, Ni and Sb are 6.37×10^{-3}, 1.15×10^{-1}, 1.16×10^{-1}, and 3.07×10^{-1} a_0^2 ($a_0^2 = 2.8002852 \times 10^{-21}$ m^2), respectively, according to the NIST Electron Elastic-Scattering Cross-Section Database, SRD 64 (https://srdata.nist.gov/srd64/). Therefore, Li/Sb mixing atom and Ni/Mn mixing atom in the ratio of 1:1 have the average scattering sections of 1.57×10^{-1} and 1.16×10^{-1} a_0^2, respectively. We can predict the alternate stacking of two dark atomic layers and one bright

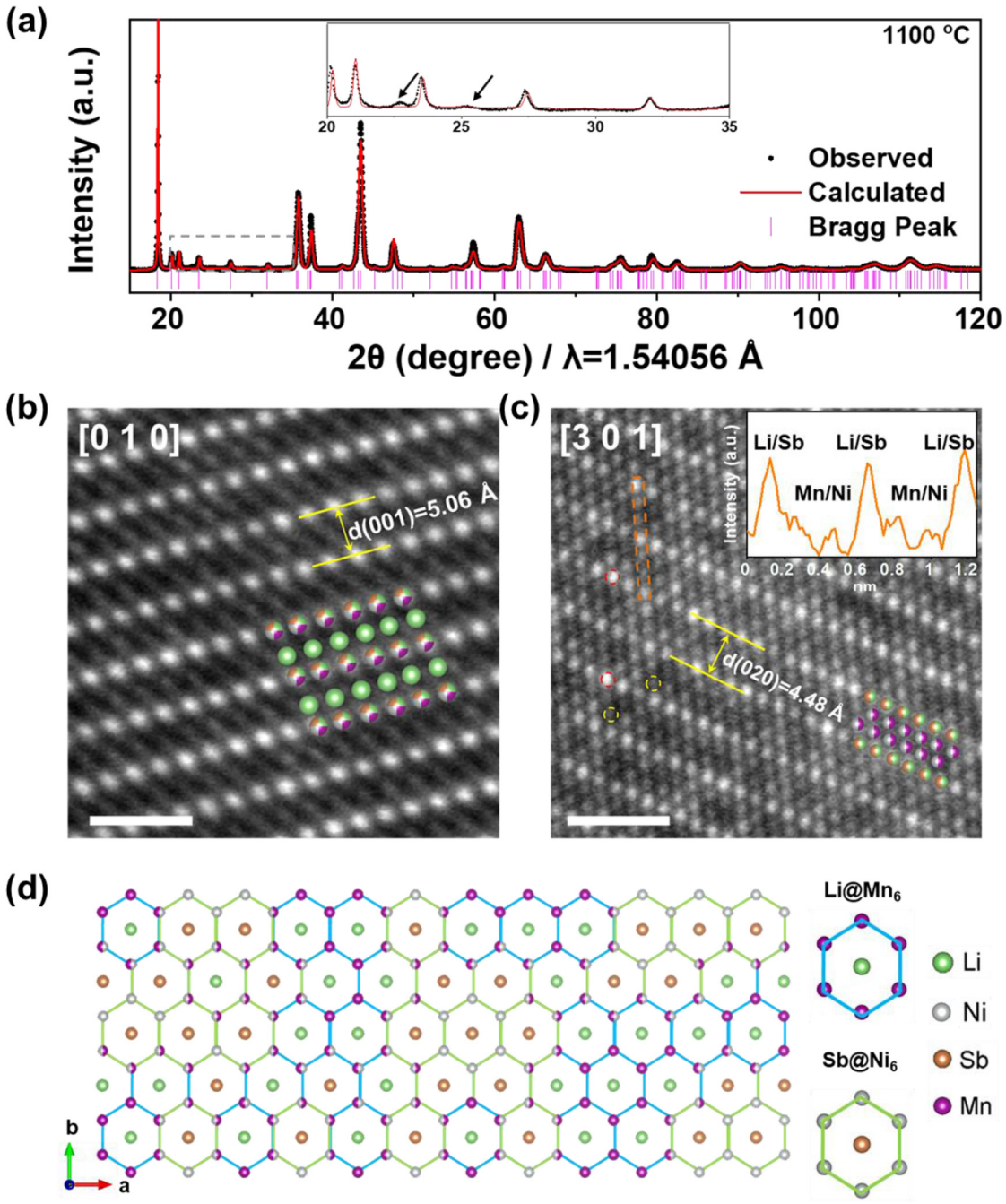

Fig. 3. Identifying the final dispersion degree of Li@Mn_6 superstructure units in the solid solution. (a) XRD pattern and the corresponding structure refinement of the solid solution LMNSO-1100. The superlattice peaks are marked by grey dashed rectangle. HAADF-STEM images of LMNSO-1100 oxide along [010] (b) and [301] direction (c). The scale bar in (b) and (c) is 1 nm. (d) The atomic illustration of the distribution of Li@Mn_6 superstructure units in the TM layer of the solid solution LMNSO-1100.

atomic layer in the HADDF-STEM image along [301] direction, which well matches with the experimental result (Fig. 3c). The intensity profile along the dashed line (inset) further confirms the deduction. A small amount of over-dark spots (marked by yellow dashed circles) can be observed in Ni/Mn mixing atomic layers, which may correspond to a small quantity of Li/TM mixing atoms. Similarly, some over-bright spots in Li/Sb mixing atomic layers (marked by red dashed circles) correspond to the Li/TM mixing atoms. On the whole, Li@Mn_6 superstructure units and Sb@Ni_6 superstructure units are uniformly mixed in TM layers of LMNSO.

Based on the results above, the atomic structure of one TM layer of LMNSO-1100 can be illustrated in Fig. 3d. Li@Mn_6 superstructure units have been uniformly dispersed in the whole TM layer, which is different from the previously reported Li-rich layered oxides. Such dispersion of Li@Mn_6 superstructure units may greatly affect the local environment of lattice oxygen, thereby the oxygen activation process in the solid solution LMNSO-1100.

3.3. *Impacts of the Li@Mn_6 dispersion on the electrochemistry*

As mentioned above, the dispersion degree of Li@Mn_6 gradually increased with the raised temperature. Therefore, we can test their electrochemical performance to evaluate the impacts of the Li@Mn_6 dispersion on oxygen activation. Fig. 4**a** presents the capacity-voltage profiles of

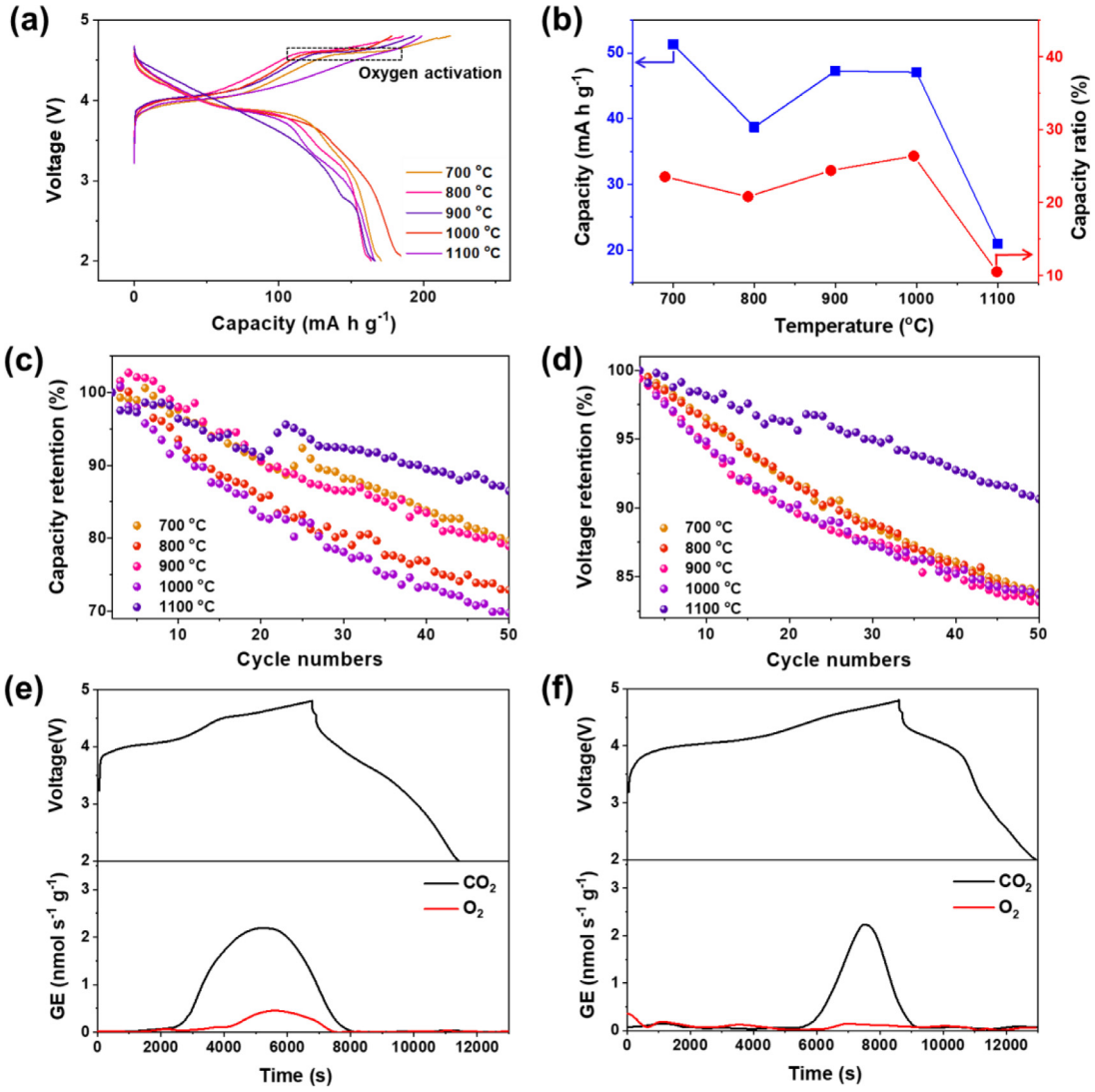

Fig. 4. The enhanced electrochemical performance by the dispersion of Li@Mn_6 superstructure units. (a) Capacity-voltage profiles at the first cycle of the LMNSO-700, LMNSO-800, LMNSO-900, LMNSO-1000 and LMNSO-1100 cathodes. (the current density is 20 mA g^{-1}) The plateau related to the oxygen activation is marked by the black dashed rectangle. (b) The specific capacity from 4.55 to 4.65 V at the first charging and the corresponding capacity ratio in fully charging capacity according to (a). (c) Capacity retention and (d) average voltage retention of LMNSO-700 to LMNSO-1100 cathodes during 50 cycles. Gas evolution during the first cycle of LMNSO-1000 (e) and LMNSO-1100 (f) determined by operando DEMS.

five cathodes in the first cycle. One slope below 4.5 V and one plateau above 4.5 V could be observed in the first charge curves for LMNSO-700, LMNSO-800, LMNSO-900 and LMNSO-1000, corresponding to Ni oxidation in LNSO component and oxygen activation in LMO component, respectively. For the discharge curves, a short plateau around 3.8 V and a slope below 3.6 V could be discovered, which were respectively related to Ni and Mn reduction. O redox occurred through the discharge process [50]. Therefore, the electrochemical behaviors of these four cathodes consist of the respective electrochemical behavior of LMO and LNSO. Differently, the solid solution LMNSO-1100 has no obvious charge plateau around 4.5 V and no obvious discharge plateau around 3.8 V, and the whole charge/discharge curve became sloping, demonstrating a solid solution effect on the electrochemistry.

To quantitatively explore the contribution of the oxygen activation to the capacity, the charge capacity from the plateau (4.55–4.65 V, related to the oxygen activation) and the ratio over the full charge capacity were displayed in Fig. 4b. The capacity contribution of the plateau related to oxygen activation was 51.32 mA h g^{-1}, 38.72 mA h g^{-1}, 47.27 mA h g^{-1}, 47.05 mA h g^{-1}, 20.89 mA h g^{-1} and the corresponding ratio was 23.54 %, 20.81 %, 24.40 %, 26.39 %, 10.51 % for LMNSO-700, LMNSO-800, LMNSO-900, LMNSO-1000 and LMNSO-1100 cathodes, respectively. A little decrease of the oxygen activation contribution from LMNSO-700 to LMNSO-800, may be due to the larger particle size of LMO from 700 to 800 °C (Fig. 1e). [51] When the temperature increases from 800 to 1000 °C, the oxygen activation contribution constantly increases, implying a better oxygen activation in LMO while Li@Mn_6 gradually migrates into LNSO particles and form the smaller nano-domains (Fig. 1e) [23]. Surprisingly, there is negligible contribution to oxygen activation for LMNSO-1100. It hints that the oxygen activation can be greatly restricted when Li@Mn_6 superstructure units are uniformly dispersed in TM layers. The similar phenomenon could also be found in CV curves, showing a much weaker oxygen activation peak at around 4.6 V for LMNSO-1100 than those for other samples (Fig. S12). To further demonstrate the relationship between the oxygen activation process and the dispersion of Li@Mn_6, a series of LMO-LNSO solid solution cathode materials with different phase ratios have been prepared (see the detailed synthetic process in Experimental section), and the corresponding XRD patterns are shown in Fig. S13. Only one set of peaks belonged to layered

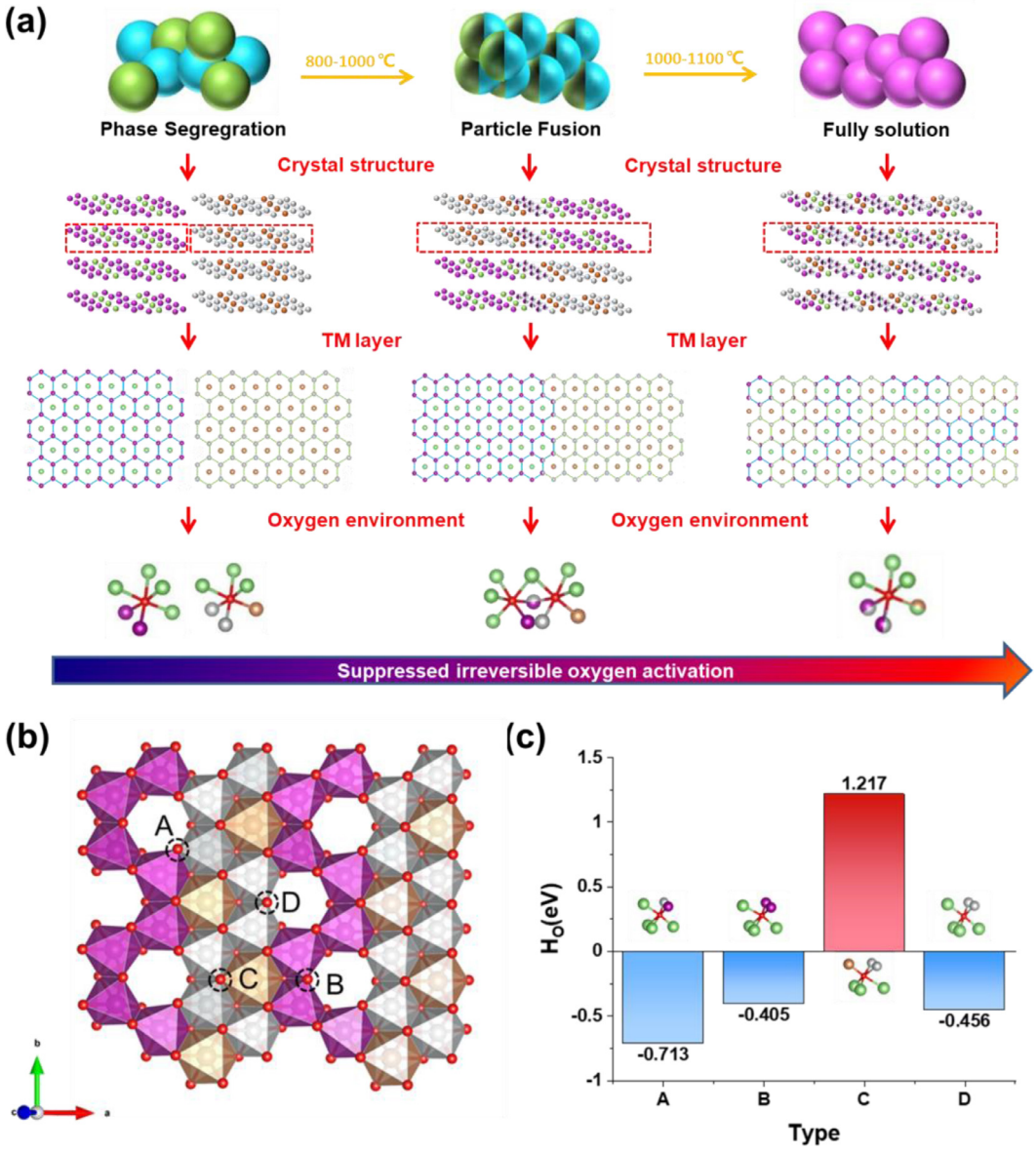

Fig. 5. Correlating the dispersion of Li@Mn_6 superstructure units with the suppressed irreversible oxygen activation. (a) Illustration of the relationship between the dispersion of Li@Mn_6 superstructure units and the electrochemical performance. (b) The structural model of LMNSO under delithiation state, and the selected oxygen atoms with different configurations. (c) The oxygen vacancy formation enthalpies for the selected oxygen atoms in LMNSO.

structure could be observed, implying the formation of solid solution in LMNSO14, LMNSO12, LMNSO21 and LMNSO41. The corresponding electrochemical performance is shown in Fig. S14. The charging plateau related to the oxygen activation gradually prolongs with the increase of LMO content (Fig. S14a), implying the oxygen activation has been suppressed with the increase of LNSO content. In Fig. S14b, the contribution of the oxygen activation to the whole charging capacity nonlinearly decreases with the decrease of LMO content. Since the decrease of LMO content means the increase of Li@Mn_6 dispersion, it could be further demonstrated that the oxygen activation process has been partly suppressed by the more dispersion of Li@Mn_6.

The capacity stability of LMNSO-700 to LMNSO-1100 cathodes is shown in Fig. 4c and the corresponding specific capacity is exhibited in Fig. S15a. LMNSO-1100 with the largest Li@Mn_6 dispersion and the least contribution to oxygen activation provides the best capacity retention of 86.50 % after 50 cycles, much larger than the other four cathodes (79.63 %, 72.91 %, 78.89 %, and 69.77 % respectively). The average discharge voltage changes are shown in Figs. S15b and 4d. The average voltage retention of LMNSO-1100 cathode was more than 92 %, larger than other cathodes (around 83%). Therefore, we can deduce that, the dispersion of Li@Mn_6 superstructure unit in TM layers can suppress the irreversible oxygen activation and enhance the stability of the oxygen framework, thus increasing the capacity and average voltage retention.

Operando differential electrochemical mass spectrometry (DEMS) is a critical tool to evaluate the reversibility of oxygen activation process [52–56]. The gas evolution during the initial cycle of LMNSO-1000 and LMNSO-1100 was studied by operando DEMS. As shown in Fig. 4e, a large amount of O_2 generated from LMNSO-1000 cathode above 4.5 V. In sharp contrast, negligible O_2 release could be observed during the first cycle of LMNSO-1100 cathode, hinting the good reversibility of oxygen activation process. In addition, less CO_2 evolution could be observed in LMNSO-1100 than that in LMNSO-1000, which hints less decomposition of the electrolyte due to surface O^- species [57]. The EIS spectra of all LMNSO cathodes are shown in Fig. S16. The impedance

decreased from 700 to 800 °C, which might be related to the enhanced crystallinity. From LMNSO-800 to LMNSO-1100, the impendence constantly increased, which may be due to the increased particle size with the temperature.

3.4. The mechanistic understanding

Combined all experimental observations of structure analysis and the electrochemical performance together, the detailed dispersion process of Li@Mn_6 superstructure units as well as the resulted oxygen environment change during the solid solution process have been summarized in Fig. 5**a** to illustrate the relationship between the dispersion of Li@Mn_6 superstructure units and the electrochemistry. Initially, Li@Mn_6 superstructure units aggregate in TM layers of LMO. Two kinds of intrinsic oxygen environments in LMO and LNSO, Li_3OMn_2Li and Li_3ONi_2Sb exist at this stage. With the temperature increasing, LMO particles gradually merge with LNSO particles to form heterogenous particles. Correspondingly, some novel oxygen environments formed into the phase boundary, partly suppressed the irreversible oxygen activation. As the temperature increases to 1100 °C, the fully solid solution has been completed at the atomic level, with the full dispersion of Li@Mn_6 in TM layers. Therefore, the aggregated Li-O-Li connection in LMO has been dispersed into LMNSO (Fig. S17) and the corresponding oxygen environment became complicated $Li_3O(Ni/Mn)_2(Li/Sb)$, which decreased the irreversible oxygen activation to a large extent, according to the previous theoretical calculations [58,59]. In one word, the dispersion of Li@Mn_6 alters the local oxygen environment from the active Li_3OMn_2Li to the less active $Li_3O(Ni/Mn)_2(Li/Sb)$, which suppresses the irreversible oxygen activation process, inhibits the severe oxygen loss and consequently alleviates the capacity and voltage decay.

The first-principles calculations were conducted to further confirm the formation enthalpy of O vacancy in LMO, LNSO and LMNSO. The structure models under delithiation state are presented in Figs. S18,S19 and Fig. 5b. In LMO, the formation enthalpies for two types of oxygen vacancy are -0.941 and -0.726 eV (Table S3), respectively, indicating the spontaneous formation of oxygen vacancies. In contrast, the oxygen vacancy formation enthalpies in LNSO are 1.226 and 1.141 eV (Table S4), indicating the stable oxygen framework. In LMNSO, there are a variety of oxygen environments (Fig. 5b). We selected four types of oxygen configurations (Fig. 5c) and calculated the oxygen vacancy formation enthalpies. The oxygen with the O-$SbNi_2$ configuration has a much larger Ho (1.217 eV), hinting that, such oxygen species can act as 'anchors' in LMNSO to suppress the migration of oxygen vacancy and the irreversible lattice oxygen activation, thus improving the structural stability. It is consistent with the improved cycling stability in LMNSO solid solution above.

4. Conclusion

The detailed crystal growth and the solid solution process of Li@Mn_6 in LMNSO from 500 to 1100 °C were explored by combining XRD and *in-situ/ex-situ* TEM with the corresponding EDS. (1) the separate nucleation of LMO and LNSO from 500 to 700 °C with Li@Mn_6 superstructure units aggregating in LMO particle; (2) the separate growth of LMO and LNSO particles from 700 to 800 °C with more aggregation of Li@Mn_6 superstructure units in bigger LMO particles; (3) Particle fusion between LMO particle and LNSO particle from 800 to 1000 °C with the decreased aggregation of Li@Mn_6 superstructure units; (4) Complete solid solution from 1000 to 1100 °C with the uniform dispersion of Li@Mn_6 superstructure units. Such dispersion of Li@Mn_6 superstructure units changed local oxygen environments and suppressed the irreversible oxygen activation. Therefore, less oxygen loss and better cycling stability were achieved at the largest dispersion degree of Li@Mn_6. Our work correlates the dispersion of Li@Mn_6 superstructure units with the oxygen activation and the cycling performance of Li-rich layered cathodes, providing guidance for the structure design of the highly stable Li-rich layered cathode for Li-ion batteries.

Declaration of Competing Interest

The authors declare that they have no known competing financial interests or personal relationships that could have appeared to influence the work reported in this paper.

CRediT authorship contribution statement

Yiwei Li: Conceptualization, Investigation, Visualization, Methodology, Formal analysis, Writing – original draft. **Shenyang Xu:** Investigation, Visualization, Methodology, Formal analysis. **Wenguang Zhao:** Investigation, Visualization, Formal analysis. **Zhefeng Chen:** Methodology. **Zhaoxi Chen:** Formal analysis. **Shunning Li:** Methodology. **Jiangtao Hu:** Resources. **Bo Cao:** Resources. **Jianyuan Li:** Formal analysis. **Shisheng Zheng:** Investigation. **Ziwei Chen:** Investigation. **Taolue Zhang:** Investigation. **Mingjian Zhang:** Conceptualization, Investigation, Writing – review & editing. **Feng Pan:** Writing – review & editing, Supervision, Project administration, Funding acquisition.

Acknowledgments

The authors acknowledge support from the National Key R&D Program of China (2016YFB0700600), the Shenzhen Science and Technology Research Grant (No. JCYJ20200109140416788), the Chemistry and Chemical Engineering Guangdong Laboratory (Grant No.1922018), the National Natural Science Foundation of China (52172175), and the National Key R&D Program of China (2020YFB0704500).

Supplementary materials

Supplementary material associated with this article can be found, in the online version, at doi:10.1016/j.ensm.2021.12.003.

Reference

[1] F. Wu, J. Maier, Y. Yu, Guidelines and trends for next-generation rechargeable lithium and lithium-ion batteries, Chem. Soc. Rev. 49 (5) (2020) 1569–1614.
[2] D. Larcher, J.M. Tarascon, Towards greener and more sustainable batteries for electrical energy storage, Nat. Chem. 7 (1) (2015) 19–29.
[3] P.K. Nayak, E.M. Erickson, F. Schipper, T.R. Penki, N. Munichandraiah, P. Adelhelm, H. Sclar, F. Amalraj, B. Markovsky, D. Aurbach, Review on challenges and recent advances in the electrochemical performance of high capacity Li- and Mn-rich cathode materials for Li-ion batteries, Adv. Energy Mater. 8 (8) (2018) 201702397.
[4] R. Schmuch, R. Wagner, G. Horpel, T. Placke, M. Winter, Performance and cost of materials for lithium-based rechargeable automotive batteries, Nat. Energy 3 (4) (2018) 267–278.
[5] M. Li, J. Lu, Z. Chen, K. Amine, 30 years of lithium-ion batteries, Adv. Mater. 30 (33) (2018) 201800561.
[6] V. Etacheri, R. Marom, R. Elazari, G. Salitra, D. Aurbach, Challenges in the development of advanced Li-ion batteries: a review, Energy Environ. Sci. 4 (9) (2011) 3243–3262.
[7] W. Lee, S. Muhammad, C. Sergey, H. Lee, J. Yoon, Y.M. Kang, W.S. Yoon, Advances in the cathode materials for lithium rechargeable batteries, Angew. Chem. Int. Ed. 59 (7) (2020) 2578–2605.
[8] W.D. Li, B.H. Song, A. Manthiram, High-voltage positive electrode materials for lithium-ion batteries, Chem. Soc. Rev. 46 (10) (2017) 3006–3059.
[9] S. Zhao, K. Yan, J. Zhang, B. Sun, G. Wang, Reaction mechanisms of layered lithium-rich cathode materials for high-energy lithium-ion batteries, Angew. Chem. Int. Ed. 60 (5) (2021) 2208–2220.
[10] Q. Li, D. Zhou, L. Zhang, D. Ning, Z. Chen, Z. Xu, R. Gao, X. Liu, D. Xie, G. Schumacher, X. Liu, Tuning anionic redox activity and reversibility for a high-capacity Li-rich Mn-based oxide cathode via an integrated strategy, Adv. Funct. Mater. 29 (10) (2019) 201806706.
[11] H.F. Zheng, X. Han, W.B. Guo, L. Lin, Q.S. Xie, P.F. Liu, W. He, L.S. Wang, D.L. Peng, Recent developments and challenges of Li-rich Mn-based cathode materials for high-energy lithium-ion batteries, Mater. Today Energy 18 (2020) 100518.
[12] S. Han, Y. Xia, Z. Wei, B. Qiu, L. Pan, Q. Gu, Z. Liu, Z. Guo, A comparative study on the oxidation state of lattice oxygen among $Li_{1.14}Ni_{0.136}Co_{0.136}Mn_{0.544}O_2$, Li_2MnO_3, $LiNi_{0.5}Co_{0.2}Mn_{0.3}O_2$ and $LiCoO_2$ for the initial charge–discharge, J. Mater. Chem. A 3 (22) (2015) 11930–11939.

[13] M. Oishi, C. Yogi, I. Watanabe, T. Ohta, Y. Orikasa, Y. Uchimoto, Z. Ogumi, Direct observation of reversible charge compensation by oxygen ion in Li-rich manganese layered oxide positive electrode material, $Li_{1.16}Ni_{0.15}Co_{0.19}Mn_{0.50}O_2$, J. Power Sources 276 (2015) 89–94.

[14] A.J. Naylor, E. Makkos, J. Maibach, N. Guerrini, A. Sobkowiak, E. Bjorklund, J.G. Lozano, A.S. Menon, R. Younesi, M.R. Roberts, K. Edstrom, M.S. Islam, P.G. Bruce, Depth-depoxygeendent n redox activity in lithium-rich layered oxide cathodes, J. Mater. Chem. A 7 (44) (2019) 25355–25368.

[15] X. Li, Y. Qiao, S. Guo, Z. Xu, H. Zhu, X. Zhang, Y. Yuan, P. He, M. Ishida, H. Zhou, Direct visualization of the reversible O^{2-} /O^{-} redox process in Li-rich cathode materials, Adv. Mater. 30 (14) (2018) 201705197.

[16] S. Muhammad, H. Kim, Y. Kim, D. Kim, J.H. Song, J. Yoon, J.H. Park, S.J. Ahn, S.H. Kang, M.M. Thackeray, W.S. Yoon, Evidence of reversible oxygen participation in anomalously high capacity Li- and Mn-rich cathodes for Li-ion batteries, Nano Energy 21 (2016) 172–184.

[17] T. Nakamura, H. Gao, K. Ohta, Y. Kimura, Y. Tamenori, K. Nitta, T. Ina, M. Oishi, K. Amezawa, Defect chemical studies on oxygen release from the Li-rich cathode material $Li_{1.2}Mn_{0.6}Ni_{0.2}O_{2-\delta}$, J. Mater. Chem. A 7 (9) (2019) 5009–5019.

[18] S. Hy, F. Felix, J. Rick, W.N. Su, B.J. Hwang, Direct in situ observation of Li_2O evolution on Li-rich high-capacity cathode material, $Li[Ni_xLi_{(1-2x)/3}Mn_{(2-x)/3}]O_2$ ($0 \le x \le 0.5$), J. Am. Chem. Soc. 136 (3) (2014) 999–1007.

[19] D. Ye, G. Zeng, K. Nogita, K. Ozawa, M. Hankel, D.J. Searles, L. Wang, Understanding the origin of Li_2MnO_3 activation in Li-rich cathode materials for lithium-ion batteries, Adv. Funct. Mater. 25 (48) (2015) 7488–7496.

[20] A.R. Armstrong, M. Holzapfel, P. Novak, C.S. Johnson, S.H. Kang, M.M. Thackeray, P.G. Bruce, Demonstrating oxygen loss and associated structural reorganization in the lithium battery cathode $Li[Ni_{0.2}Li_{0.2}Mn_{0.6}]O_2$, J. Am. Chem. Soc. 128 (26) (2006) 8694–8698.

[21] L. Riekehr, J. Liu, B. Schwarz, F. Sigel, I. Kerkamm, Y. Xia, H. Ehrenberg, Fatigue in $0.5Li_2MnO_3$:$0.5Li(Ni_{1/3}Co_{1/3}Mn_{1/3})O_2$ positive electrodes for lithium ion batteries, J. Power Sources 325 (2016) 391–403.

[22] D. Mohanty, A.S. Sefat, S. Kalnaus, J. Li, R.A. Meisner, E.A. Payzant, D.P. Abraham, D.L. Wood, C. Daniel, Investigating phase transformation in the $Li_{1.2}Co_{0.1}Mn_{0.55}Ni_{0.15}O_2$ lithium-ion battery cathode during high-voltage hold (4.5 V) via magnetic, X-ray diffraction and electron microscopy studies, J. Mater. Chem. A 1 (20) (2013) 6249–6261.

[23] Z. Zhuo, K. Dai, R. Qiao, R. Wang, J. Wu, Y. Liu, J. Peng, L. Chen, Y.D. Chuang, F. Pan, Z.X. Shen, G. Liu, H. Li, T.P. Devereaux, W. Yang, Cycling mechanism of Li_2MnO_3: Li–CO_2 batteries and commonality on oxygen redox in cathode materials, Joule 5 (2021) 975–997.

[24] J. Zheng, P. Xu, M. Gu, J. Xiao, N.D. Browning, P. Yan, C. Wang, J.G. Zhang, Structural and chemical evolution of Li- and Mn-rich layered cathode material, Chem. Mat. 27 (4) (2015) 1381–1390.

[25] D. Mohanty, S. Kalnaus, R.A. Meisner, K.J. Rhodes, J. Li, E.A. Payzant, D.L. Wood, C. Daniel, Structural transformation of a lithium-rich $Li_{1.2}Co_{0.1}Mn_{0.55}Ni_{0.15}O_2$ cathode during high voltage cycling resolved by in situ X-ray diffraction, J. Power Sources 229 (2013) 239–248.

[26] Y. Song, X. Zhao, C. Wang, H. Bi, J. Zhang, S. Li, M. Wang, R. Che, Insight into the atomic structure of Li_2MnO_3 in Li-rich Mn-based cathode materials and the impact of its atomic arrangement on electrochemical performance, J. Mater. Chem. A 5 (22) (2017) 11214–11223.

[27] J. Zhang, F. Cheng, S. Chou, J. Wang, L. Gu, H. Wang, H. Yoshikawa, Y. Lu, J. Chen, Tuning oxygen redox chemistry in Li-rich Mn-based layered oxide cathodes by modulating cation arrangement, Adv. Mater. 31 (42) (2019) 201901808.

[28] J. Hwang, S. Myeong, W. Jin, H. Jang, G. Nam, M. Yoon, S.H. Kim, S.H. Joo, S.K. Kwak, M.G. Kim, J. Cho, Excess-Li localization triggers chemical irreversibility in Li- and Mn-rich layered oxides, Adv. Mater. 32 (34) (2020) 2001944.

[29] J. Hwang, S. Myeong, E. Lee, H. Jang, M. Yoon, H. Cha, J. Sung, M.G. Kim, D.H. Seo, J. Cho, Lattice-oxygen-stabilized Li- and Mn-rich cathodes with sub-micrometer particles by modifying the excess-Li distribution, Adv. Mater. 33 (18) (2021) 2100352.

[30] Y.X. Zuo, B.A. Li, N. Jiang, W.S. Chu, H. Zhang, R.Q. Zou, D.G. Xia, A high-capacity O2-type Li-rich cathode material with a single-layer Li_2MnO_3 superstructure, Adv. Mater. 30 (16) (2018) 201707255.

[31] F. Dogan, B.R. Long, J.R. Croy, K.G. Gallagher, H. Iddir, J.T. Russell, M. Balasubramanian, B. Key, Re-entrant lithium local environments and defect driven electrochemistry of Li- and Mn-rich Li-ion battery cathodes, J. Am. Chem. Soc. 137 (6) (2015) 2328–2335.

[32] B.R. Long, J.R. Croy, F. Dogan, M.R. Suchomel, B. Key, J. Wen, D.J. Miller, M.M. Thackeray, M. Balasubramanian, Effect of cooling rates on phase separation in $0.5Li_2MnO_3$·$0.5LiCoO_2$ electrode materials for Li-ion batteries, Chem. Mat. 26 (11) (2014) 3565–3572.

[33] N. Kitamura, Y. Kubo, N. Ishida, Y. Idemoto, Study of atomic ordering across the layer in lithium-rich layered positive electrode material towards preparation process optimization, J. Power Sources 437 (2019) 226905.

[34] Z. Wang, Y. Yin, Y. Ren, Z. Wang, M. Gao, T. Ma, W. Zhuang, S. Lu, A. Fan, K. Amine, Z. Chen, High performance lithium-manganese-rich cathode material with reduced impurities, Nano Energy 31 (2017) 247–257.

[35] W.C. Chen, Y.F. Song, C.C. Wang, Y. Liu, D.T. Morris, P.A. Pianetta, J.C. Andrews, H.C. Wu, N.L. Wu, Study on the synthesis–microstructure-performance relationship of layered Li-excess nickel–manganese oxide as a Li-ion battery cathode prepared by high-temperature calcination, J. Mater. Chem. A 1 (36) (2013) 10847–10856.

[36] B.H. Toby, EXPGUI, a graphical user interface for GSAS, J. Appl. Crystallogr. 34 (2) (2001) 210–213.

[37] A.C. Larson, R.B. Dreele, B. Toby, Los Alamos National Laboratory: Los Alamos, in: General structure analysis system - GSAS/EXPGUI, LAUR, 2000, pp. 86–748.

[38] G. Kresse, J. Hafner, Ab initio molecular dynamics for liquid metals, Phys. Rev. B 47 (1) (1993) 558–561.

[39] G. Kresse, J. Furthmüller, Efficient iterative schemes for ab initio total-energy calculations using a plane-wave basis set, Phys. Rev. B 54 (16) (1996) 11169–11186.

[40] S.K. Mishra, G. Ceder, Structural stability of lithium manganese oxides, Phys. Rev. B 59 (9) (1999) 6120–6130.

[41] G. Kresse, J. Furthmüller, Efficiency of ab-initio total energy calculations for metals and semiconductors using a plane-wave basis set, Comput. Mater. Sci. 6 (1) (1996) 15–50.

[42] P.E. Blöchl, Projector augmented-wave method, Phys. Rev. B 50 (24) (1994) 17953–17979.

[43] G. Kresse, D. Joubert, From ultrasoft pseudopotentials to the projector augmented-wave method, Phys. Rev. B 59 (3) (1999) 1758–1775.

[44] J.P. Perdew, K. Burke, M. Ernzerhof, Generalized gradient approximation made simple, Phys. Rev. Lett. 77 (18) (1996) 3865–3868.

[45] S.L. Dudarev, G.A. Botton, S.Y. Savrasov, C.J. Humphreys, A.P. Sutton, Electron-energy-loss spectra and the structural stability of nickel oxide: an LSDA + U study, Phys. Rev. B 57 (3) (1998) 1505–1509.

[46] V.I. Anisimov, J. Zaanen, O.K. Andersen, Band theory and Mott insulators: Hubbard U instead of Stoner I, Phys. Rev. B 44 (3) (1991) 943–954.

[47] L. Wang, T. Maxisch, G. Ceder, A first-principles approach to studying the thermal stability of oxide cathode materials, Chem. Mater. 19 (3) (2007) 543–552.

[48] F. Zhou, M. Cococcioni, C.A. Marianetti, D. Morgan, G. Ceder, First-principles prediction of redox potentials in transition-metal compounds with LDA + U, Phys. Rev. B 70 (23) (2004) 235121.

[49] L. Wang, T. Maxisch, G. Ceder, Oxidation energies of transition metal oxides within the GGA + U framework, Phys. Rev. B 73 (19) (2006) 195107.

[50] R.A. House, U. Maitra, M.A. Perez-Osorio, J.G. Lozano, L. Jin, J.W. Somerville, L.C. Duda, A. Nag, A. Walters, K.J. Zhou, M.R. Roberts, P.G. Bruce, Superstructure control of first-cycle voltage hysteresis in oxygen-redox cathodes, Nature 577 (7791) (2020) 502–508.

[51] C.O. Ehi-Eromosele, S.O. Ajayi, C.N. Onwucha, Optimizing the electrochemical performance of Li_2MnO_3 cathode materials for Li-ion battery using solution combustion synthesis: higher temperature and longer syntheses improves performance, J. Alloy. Compd. 861 (2021) 157972.

[52] J. Vergnet, M. Saubanere, M.L. Doublet, J.M. Tarascon, The structural stability of P2-layered Na-based electrodes during anionic redox, Joule 4 (2) (2020) 420–434.

[53] J. Xu, M. Sun, R. Qiao, S.E. Renfrew, L. Ma, T. Wu, S. Hwang, D. Nordlund, D. Su, K. Amine, J. Lu, B.D. McCloskey, W. Yang, W. Tong, Elucidating anionic oxygen activity in lithium-rich layered oxides, Nat. Commun. 9 (1) (2018) 947.

[54] K. Zhou, S. Zheng, F. Ren, J. Wu, H. Liu, M. Luo, X. Liu, Y. Xiang, C. Zhang, W. Yang, L. He, Y. Yang, Fluorination effect for stabilizing cationic and anionic redox activities in cation-disordered cathode materials, Energy Storage Mater. 32 (2020) 234–243.

[55] Z. Zhu, D. Yu, Z. Shi, R. Gao, X. Xiao, I. Waluyo, M. Ge, Y. Dong, W. Xue, G. Xu, W.K. Lee, A. Hunt, J. Li, Gradient-morph $LiCoO_2$ single crystals with stabilized energy density above 3400 W h L^{-1}, Energy Environ. Sci. 13 (6) (2020) 1865–1878.

[56] W. Yang, T.P. Devereaux, Anionic and cationic redox and interfaces in batteries: advances from soft X-ray absorption spectroscopy to resonant inelastic scattering, J. Power Sources 389 (2018) 188–197.

[57] J. Liu, M. Hou, J. Yi, S. Guo, C. Wang, Y. Xia, Improving the electrochemical performance of layered lithium-rich transition-metal oxides by controlling the structural defects, Energy Environ. Sci. 7 (2) (2014) 705–714.

[58] M. Sathiya, K. Ramesha, G. Rousse, D. Foix, D. Gonbeau, A.S. Prakash, M.L. Doublet, K. Hemalatha, J.M. Tarascon, High performance $Li_2Ru_{1-y}Mn_yO_3$ ($0.2 \le y \le 0.8$) cathode materials for rechargeable lithium-ion batteries: their understanding, Chem. Mat. 25 (7) (2013) 1121–1131.

[59] D.M. Liu, X.J. Fan, Z.H. Li, T. Liu, M.H. Sun, C. Qian, M. Ling, Y.J. Liu, C.D. Liang, A cation/anion co-doped $Li_{1.12}Na_{0.08}Ni_{0.2}Mn_{0.6}O_{1.95}F_{0.05}$ cathode for lithium ion batteries, Nano Energy 58 (2019) 786–796.